Supporting Information for 'Tunable Phase Transitions and High Photovoltaic Performance of Two-Dimensional $In_2Ge_2Te_6$ Semiconductors'

Naihua Miao,[*,†,‡] Wei Li,[†] Linggang Zhu,[†] Bin Xu,[¶] Jian Zhou,[†] Stephen R. Elliott,[†,‡,§] and Zhimei Sun[*,†,‡]

†*School of Materials Science and Engineering, Beihang University, Beijing, 100191, China.*
‡*Center for Integrated Computational Materials Engineering, International Research Institute for Multidisciplinary Science, Beihang University, Beijing, 100191, China.*
¶*School of Physical Science and Technology, Soochow University, Suzhou, 215006, China.*
§*Department of Chemistry, University of Cambridge, Lensfield Road, CB2 1EW Cambridge, United Kingdom*

E-mail: nhmiao@buaa.edu.cn; zmsun@buaa.edu.cn

Table of Contents

1. Computational Methodology

***Ab initio* calculations.** Based on density-functional theory, we performed *ab initio* calculations using the projector-augmented wave method[S1] as implemented in the Vienna *ab initio* Simulation Package (VASP).[S2] The generalized gradient approximation (GGA) with Perdew-Burke-Ernzerhof parametrization (PBE)[S3] was applied for the exchange-correlation functional.[S4] To deal with the van der Waals interactions between the layers, the density functional dispersion correction (D3-Grimme)[S5] was adopted. Electronic band structures and electrostatic doping calculations were obtained by GGA-PBE (unless stated otherwise) and compared with those from the Heyd-Scuseria-Ernzerhof (HSE06) screened hybrid functional.[S6] The cut-off energy for the plane-wave basis was 400 eV. The k-meshes for the bulk and 2D crystals were 7×7×3 and 7×7×1, respectively. Energy differences of 1×10^{-6} eV in electronic self-consistent calculations and residual forces of 1×10^{-2} eV/Å on atoms were used as convergence criteria. To eliminate the interactions between adjacent layers, a vacuum of 20 Å was constructed perpendicular to the layer plane for the monolayer.

Estimation of carrier mobility. The carrier mobility (μ) was estimated from the deformation-potential theory,[S7] which has been successfully used in many 2D materials.[S8–S10] For 2D materials, the carrier mobility can be expressed as

$$\mu = \frac{2e\hbar^3 C}{3k_B T |m^*|^2 E_{DP}^2}$$

where C is the elastic modulus, defined as $C = (\partial\varepsilon/\partial\delta) \times V_0/S_0$, in which ε is the stress under uniaxial strain δ and V_0/S_0 is the volume/area of the optimized 2D structure. m^* is the effective mass of electron and hole, which can be calculated from the derivatives of electronic bands.[S11] E_{DP} is the deformation-potential constant, defined as $\Delta E = E_{DP}(\Delta l/l_0)$, where ΔE is the shift of the band-edge positions with respect to the lattice dilation $\Delta l/l_0$ along the [100] and [010] directions of the orthogonal cell (also refers to the inset of Figure 5(a)). The relaxation time of carriers can be estimated from $\tau = \mu m^*/e$.

Lattice-dynamics and molecular-dynamics simulations. The phonon-dispersion curves were calculated using 6×6×1 supercells with the finite-displacement method.[S12–S14] *Ab initio* molecular-dynamics simulations were performed at 300 K for 20 ps with a timestep of 2 fs, using the canonical ensemble (NVT) with a Nosé-Hoover thermostat.[S15,S16]

Calculation of vdW pressure. The vdW pressure of the 2D crystals was calculated from the energy per unit volume according to:

$$P_{vdW} = \frac{E - E_0}{V - V_0}$$

where $E_0(E)$ and $V_0(V)$ are the energy and volume for the free (pressured) crystals, respectively. Note that, for 2D bilayers, the pressures are mainly along the vdW axis as the surfaces are almost invariant.

Prediction of absorption coefficients. Firstly, the frequency-dependent dielectric matrices were generated from the HSE06 hybrid-functional calculations. The imaginary dielectric functions $\varepsilon_2(\omega)$ were obtained by summation over empty states:

$$\varepsilon_2(\omega) = \frac{4\pi^2 e^2}{\Omega} lim_{q \to 0} \frac{1}{q^2} \sum_{c,v,\mathbf{k}} 2w_\mathbf{k} \delta(\varepsilon_{c\mathbf{k}} - \varepsilon_{v\mathbf{k}} - \omega)$$
$$\times \langle u_{c\mathbf{k}} + e_{\alpha q}|u_{v\mathbf{k}}\rangle \langle u_{c\mathbf{k}} + e_{\beta q}|u_{v\mathbf{k}}\rangle^*$$

where c and v are conduction- and valence-band states, respectively, and $u_{c\mathbf{k}}$ is the cell periodic part of the orbitals at the k-point $\mathbf{k}$. The real dielectric matrices $\varepsilon_1(\omega)$ were calculated according to the usual Kramers-Kronig transformation:[S17–S19]

$$\varepsilon_1(\omega) = 1 + \frac{2}{\pi} P \int_0^\infty \frac{\varepsilon_2(\omega')\omega'}{\omega'^2 - \omega^2 + i\eta} d\omega'$$

where P denotes the principal value. Finally, the optical-absorption coefficients were derived

from these dielectric functions:[S18]

$$\alpha(\omega) = \sqrt{2}\omega[\sqrt{\varepsilon_1^2(\omega) + \varepsilon_2^2(\omega)} - \varepsilon_1(\omega)]^{1/2}.$$

To include excitonic effects, the time-dependent Hartree-Fock approach (TDHF) was also used to calculate the frequency-dependent dielectric matrices[S20] and obtain the optical spectra as indicated.

Simulation of power-conversion efficiency. For a solar cell, the power-conversion efficiency is defined as $P_m/P_{in} \times 100\%$, where P_m is the maximum output power density and P_{in} is the total incident solar-energy density from the solar spectrum. P_m can be obtained by maximizing the product of the current density J and voltage V:[S21,S22]

$$P = JV = (J_{sc} - J_0(e^{eV/k_BT} - 1))V,$$

where J_{sc} is the short-circuit current density and J_0 is the reverse-saturation current density, which are given by:

$$J_{sc} = e \int_0^\infty a(E)I_{sun}(E)dE,$$

$$J_0 = \frac{J_0^r}{f_r} = \frac{e\pi}{f_r} \int_0^\infty a(E)I_{bb}(E,T)dE.$$

They can be calculated from the absorptivity $a(E)$, the AM1.5G solar spectrum $I_{sun}(E)$, the black-body spectrum $I_{bb}(E,T)$ as well as the fraction of the radiative recombination current f_r accordingly:

$$a(E) = 1 - e^{-2\alpha(\omega)L},$$

$$f_r = e^{-(E_g^{da} - E_g)/k_BT},$$

where $\alpha(\omega)$ is the absorption coefficient and L is the thickness of the absorber layer; E_g

and E_g^{da} are fundamental and direct-allowed bandgaps, respectively. For direct bandgap absorbers, f_r=1; while for crystalline silicon, a more reasonable f_r is set to 10^{-3}.[S23–S26]

Simulation reliability test. To assess the reliability of the present simulations, we have briefly compared the benchmark of our calculations with previous experimental and theoretical studies, as summarized in Table S4 and Figure S9. Good agreement has been achieved for lattice parameters and the vdW gap of bulk $In_2Ge_2Te_6$, the exfoliation energy of graphite, absorption spectra (Figure 4(a)) and the SLME photovoltaic efficiency of bulk GaAs and Si crystals, indicating that our calculations are valid and reliable within the present theoretical frameworks.

2. Calculated electronic band structure of bulk In$_2$Ge$_2$Te$_6$
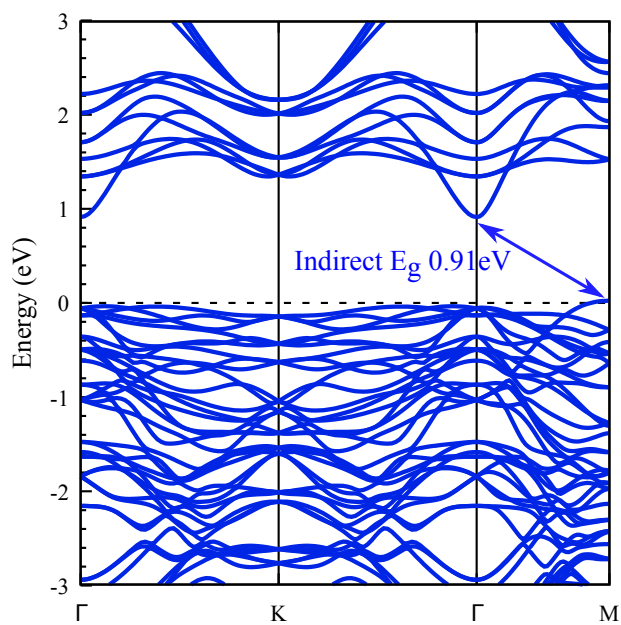
Figure S1 Calculated electronic band structure of the bulk crystal. The Fermi energy is set to 0 eV.

3. Simulated mechanical cleavage process of the $In_2Ge_2Te_6$ crystals compared with graphite
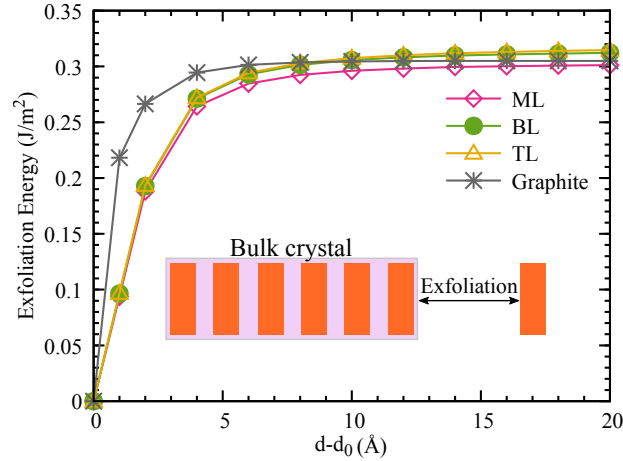
Figure S2 Calculated exfoliation energy vs separation distance $d - d_0$ in comparison with graphite, where d_0 is the vdW gap between adjacent layers of the bulk crystals and d is the distance between the exfoliated layer and the surface of the bulk.

In the simulation, the monolayer (bilayer/trilayer) was moved away from the surface of the thick-bulk cell by increasing d, that is the distance between the exfoliated layer and the bulk surface. At each d, we calculated the total energy difference, $E_d - E_{d0}$, which would converge at some distance (usually less than 20 Å). The converged value $(E_d - E_{d0})$/surface-area is the simulated exfoliation energy.

4. Magnetic structures and total energies for the single-layer 2×2×1 supercells
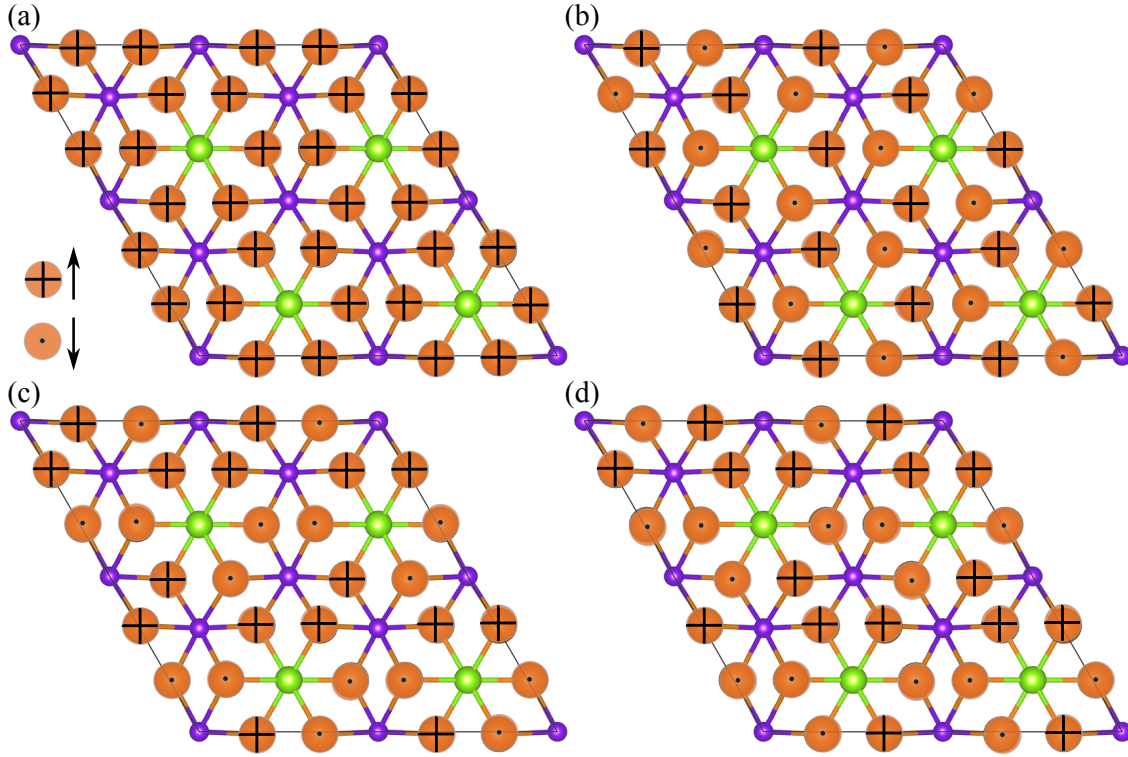
Figure S3 Magnetic configurations with oriented up (↑) and down (↓) spins on tellurium atoms being considered: (a) ferromagnetic (FM), (b) antiferromagnetic (AFM-1), (c) antiferromagnetic (AFM-2), and (d) antiferromagnetic (AFM-3) states. The magnetic moments of indium and germanium atoms are close to zero as the magnetic properties are dominated by the Te-$5p$ orbitals.

The atomic positions (x, y, z) and lattice constants $(2a)$ of single-layer supercells were fully relaxed and it is not evident that the structures are buckling, as there are competing atomic motions under electrostatic doping.

5. Spin-resolved projected electronic density of states of the In$_2$Ge$_2$Te$_6$ monolayer under electrostatic doping
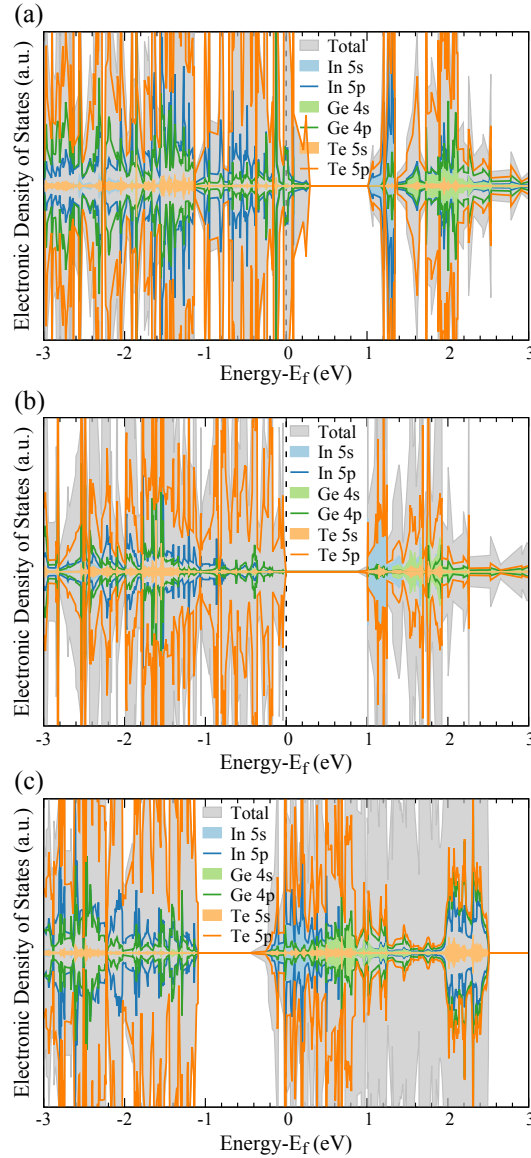
Figure S4 Spin-resolved projected density of states at (a) 3.4×10^{14} cm^{-2} hole doping, (b) neutral, and (c) 2.6×10^{14} cm^{-2} electron doping, corresponding to nonmagnetic metal, nonmagnetic semiconductor, and antiferromagnetic metal, respectively. The Fermi level is marked by a dashed line, and is set to lie at 0 eV.

Table S1 Calculated magnetic quantities for the 2×2×1 supercells of In$_2$Ge$_2$Te$_6$ monolayer: number of carriers No. (electron/supercell, negative value indicates hole/supercell), lattice constant 2a (Å), carrier density ρ (10^{13}cm^{-2}), magnetic energy $E_{Mag.}$ (total energy difference between ground state (GS) and nonmagnetic (NM) state, meV/supercell) and magnetic ground state. The structures were relaxed for each value of carrier number. The resulting small structural relaxations are responsible for the corresponding small differences in carrier density for electrons and holes for a given carrier number.

Carrier number No. (electron)	Lattice constant 2a (Å)	Carrier density ρ (10^{13}cm^{-2})	$E_{GS} - E_{NM}$ $E_{mag.}$ (meV)	Ground state
-7.5	14.403	-41.75	-2.6	FM Metal
-7.0	14.322	-39.40	-8.0	FM Metal
-6.5	14.258	-36.92	-2.2	FM Metal
-6.0	14.206	-34.33	0.0	NM Metal
-5.0	14.123	-28.95	0.0	NM Metal
-4.5	14.103	-26.13	0.0	NM Metal
-4.0	14.098	-23.24	0.0	NM Metal
-3.5	14.107	-20.31	0.0	NM Metal
-3.0	14.128	-17.35	0.0	NM Metal
-2.5	14.160	-14.40	0.0	NM Metal
-2.0	14.193	-11.46	0.0	NM Metal
-1.5	14.232	-8.55	0.0	NM Metal
-1.0	14.277	-5.67	0.0	NM Metal
-0.5	14.335	-2.81	0.0	NM Metal
0.0	14.402	0.00	0.0	NM Semiconductor
0.5	14.456	2.76	0.0	NM Metal
1.0	14.515	5.48	0.0	NM Metal
1.5	14.611	8.11	0.0	NM Metal
2.0	14.630	10.79	-14.1	FM Metal
2.5	14.669	13.42	-18.4	FM Metal
3.0	14.702	16.03	-16.9	FM Metal
3.5	14.736	18.61	-4.0	FM Metal
4.0	14.771	21.17	-10.1	AFM Metal
4.5	14.792	23.75	-23.3	AFM Metal
5.0	14.824	26.27	-39.3	AFM Metal
6.0	14.879	31.30	-63.8	AFM Metal
7.0	14.942	36.20	-40.9	AFM Metal
8.0	15.004	41.03	-4.3	AFM Metal

6. Electronic structures of In$_2$Ge$_2$Te$_6$ bilayers under vdW pressure

(a) AA Stacking

-0.5   +0.5
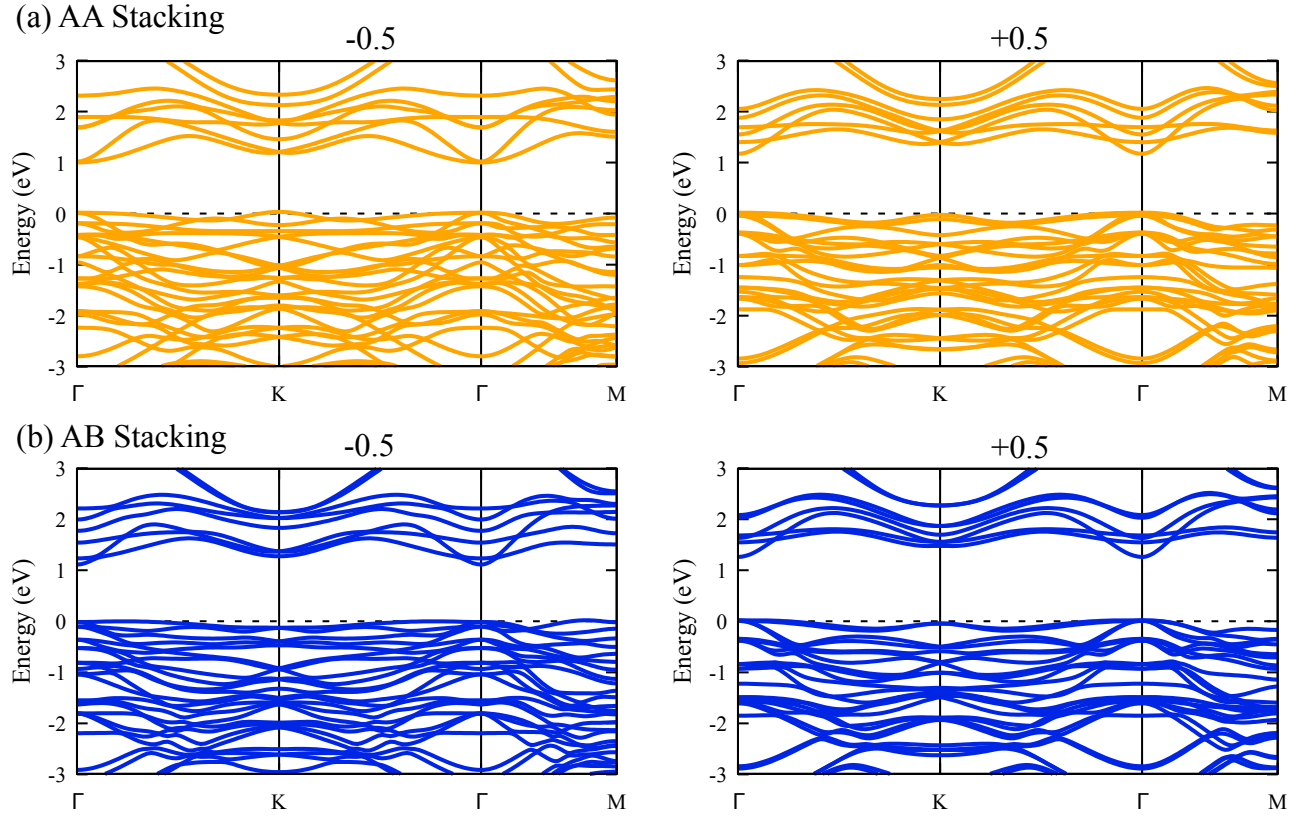
(b) AB Stacking

-0.5   +0.5

Figure S5 Calculated electronic band structures of (a) AA- and (b) AB-stacking bilayers under compressive and tensile pressure, where ΔvdW=-0.5, +0.5 Å.

Figure S5 shows that the shapes of electronic structures in both phases do not change significantly under vdW pressures, while the electronic bandgaps and SLME decrease slightly with an increase of pressure (Table S2).

Table S2 Calculated electronic bandgap and SLME of AA- and AB-stacking bilayers under compressive and tensile pressure, where ΔvdW=-0.5, +0.5 Å.

ΔvdW (Å)	E_g (eV)		SLME (%)	
	AA	AB	AA	AB
-0.5	0.99	1.10	30.00	31.68
0.0	1.17	1.21	32.04	32.10
+0.5	1.23	1.25	31.89	31.86

7. Calculated electronic band edges and SLME of the In$_2$Ge$_2$Te$_6$ monolayer under various strains
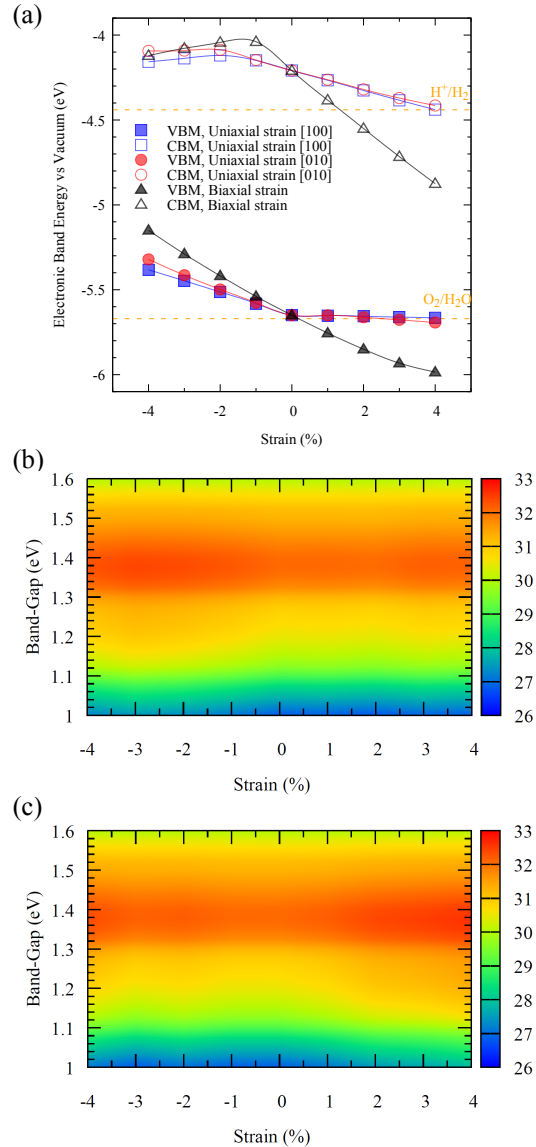
Figure S6 (a) Calculated electronic band-edge alignments of the monolayer under various strains with respect to vacuum using the HSE06 functional. The redox potentials of water splitting at pH=0 are indicated by orange dotted lines. (b) and (c) SLME maps of the monolayer crystals under uniaxial strains along [100] and [010] directions, respectively.

Under a tensile biaxial strain of 1%, the band edges of the monolayer cover the redox potentials, indicating that it is a potential photocatalyst for water splitting.

8. Calculated absorption spectra of the In$_2$Ge$_2$Te$_6$ monolayer under biaxial strains
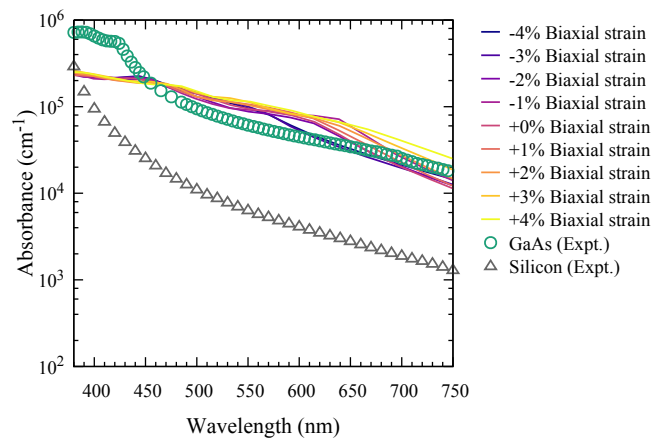
Figure S7 Calculated optical absorption of the monolayer under biaxial strains using HSE06 functional in comparison with GaAs[S27] and silicon[S28] crystals.

9. Calculated electronic bandgap, edges, and SLME of the AB-stacked $In_2Ge_2Te_6$ bilayer under various strains
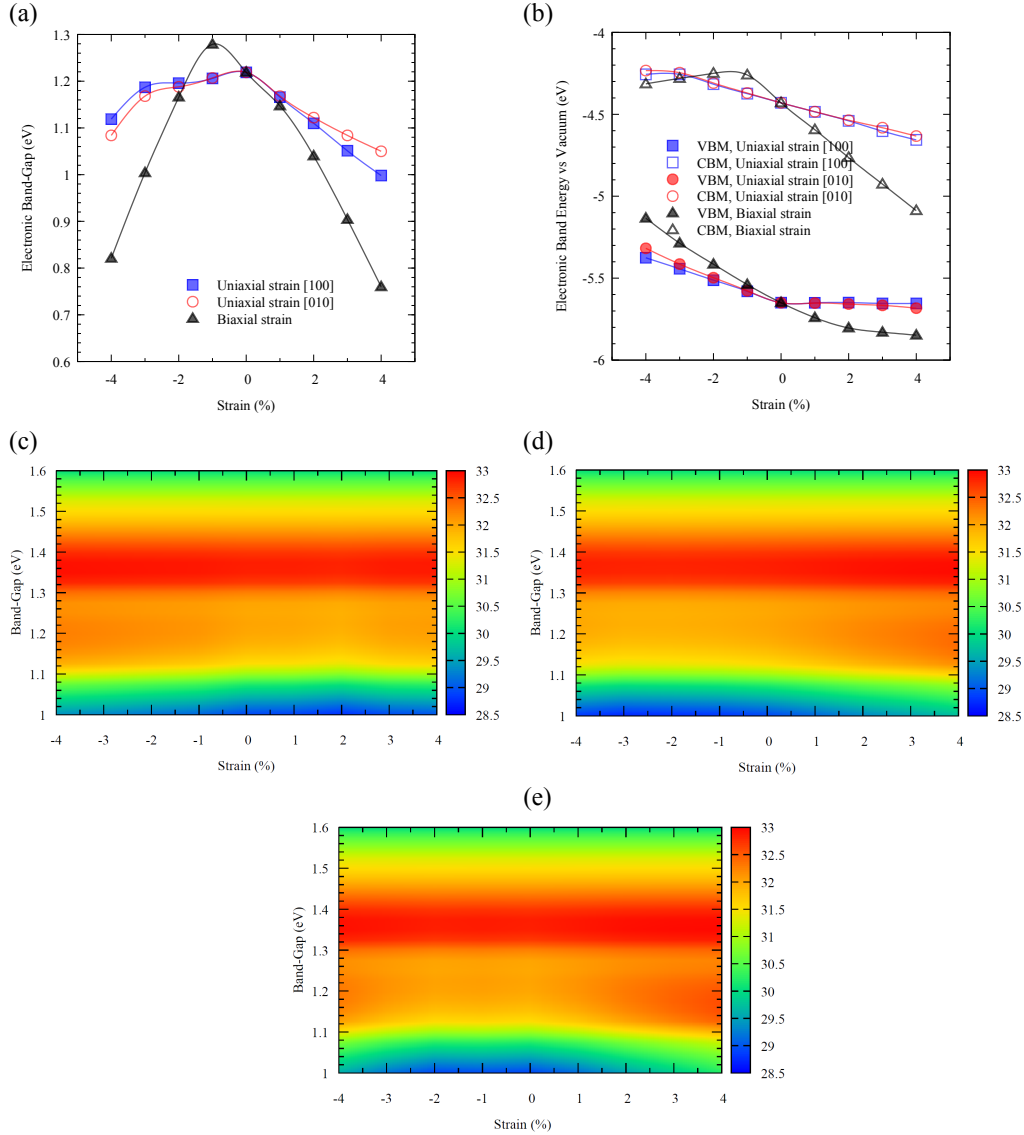
Figure S8 (a) Calculated electronic band gap and (b) edge alignments of the AB-stacked bilayer under various strains with respective to vacuum, using the HSE06 functional. (c), (d) and (e) are SLME maps of the bilayer crystals under [100] uniaxial strains, [010] uniaxial strains, as well as biaxial strains, respectively.

10. Excitonic effects on the simulated SLME

Table S3 Calculated SLME of few-layer $In_2Ge_2Te_6$ and GaAs with/without considering excitonic effects using the HSE06 and TDHF methods.

	SLME (%)	
	HSE06	TDHF
ML	31.64	31.82
BL-AB	31.86	32.10
TL-ABC	31.94	32.17
Bulk	28.63	28.83
GaAs	31.30	31.43

According to the simulations in Table S3, the SLME of these materials slightly increases ($\sim 0.2\%$) when considering the excitonic effects.

11. Reliability of the present simulations

Table S4 Calculated lattice parameters (a and c, Å) and van der Waals gap (Å) of bulk In$_2$Ge$_2$Te$_6$, exfoliation energy (EE, J/m^2) of graphite, and highest SLME photovoltaic efficiency (PE) of GaAs and silicon, in comparison with available theoretical and experimental data.

Content	This Work	Other Theory	Experiment
In$_2$Ge$_2$Te$_6$ a	7.203	-	7.086[S29]
In$_2$Ge$_2$Te$_6$ c	21.485	-	21.206[S29]
In$_2$Ge$_2$Te$_6$ vdW Gap	3.315	-	3.282[S29]
Graphite EE	0.31	0.32[S30]	0.32±0.03[S31]
GaAs PE	31.4%	32.0%[S32]	29.1%[S33]
Si PE	25.7%	25.0%[S26]	26.1%[S33]
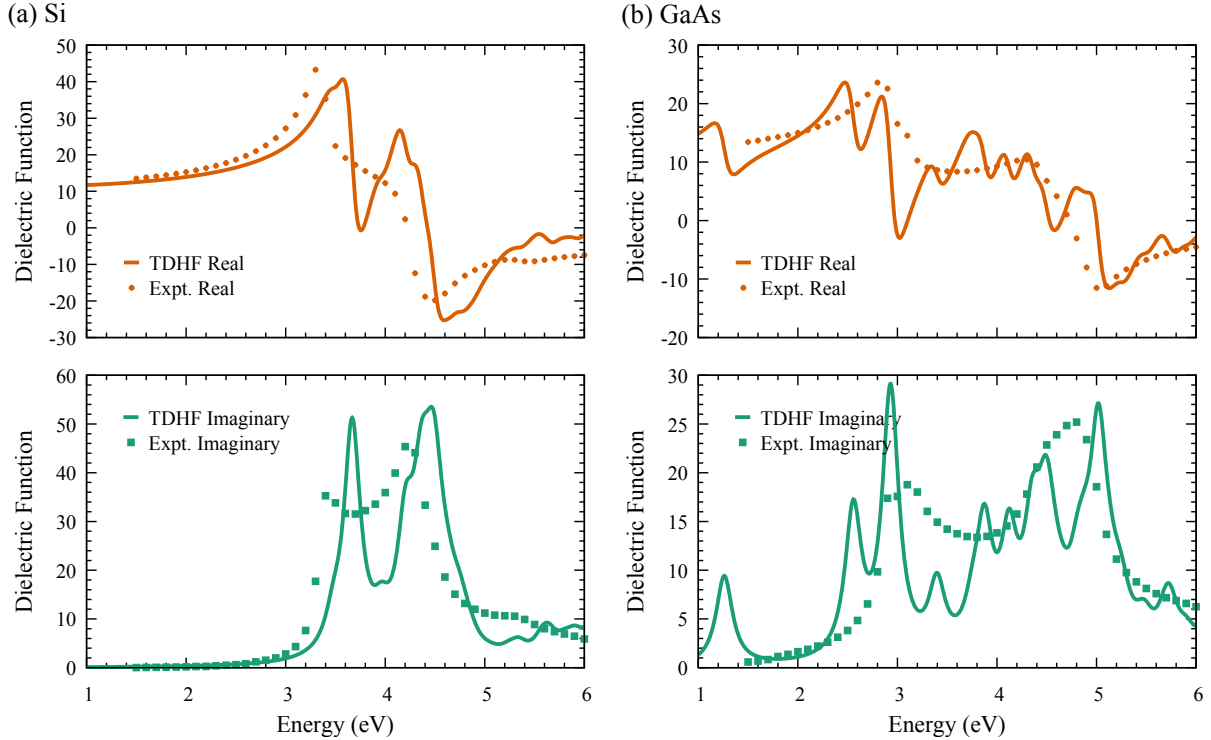
Figure S9 Calculated dielectric functions of Si and GaAs using time-dependent Hartree-Fock (TDHF) method in comparison with experimental data.[S34]

Good agreement between our simulation and experiment has been achieved for the lattice parameters and the vdW gap (Table S4) of bulk In$_2$Ge$_2$Te$_6$. The calculated exfoliation energy of graphite is very close to the previous theoretical and experimental results. The calculated dielectric functions (Figure S9) and photovoltaic efficiency of GaAs and Si are in reasonable

agreement with previous experimental measurements, where the small discrepancies can be understood as being due to the surface roughness of crystal samples and temperature effects, which are not included in this work. Therefore, our simulations are valid and reliable within the present theoretical framework in comparison with available experimental and theoretical studies.

12. Calculated dielectric functions of few-layer $In_2Ge_2Te_6$

(a) Bulk

(b) TL-ABC

(c) BL-AA

(d) BL-AB

(e) ML
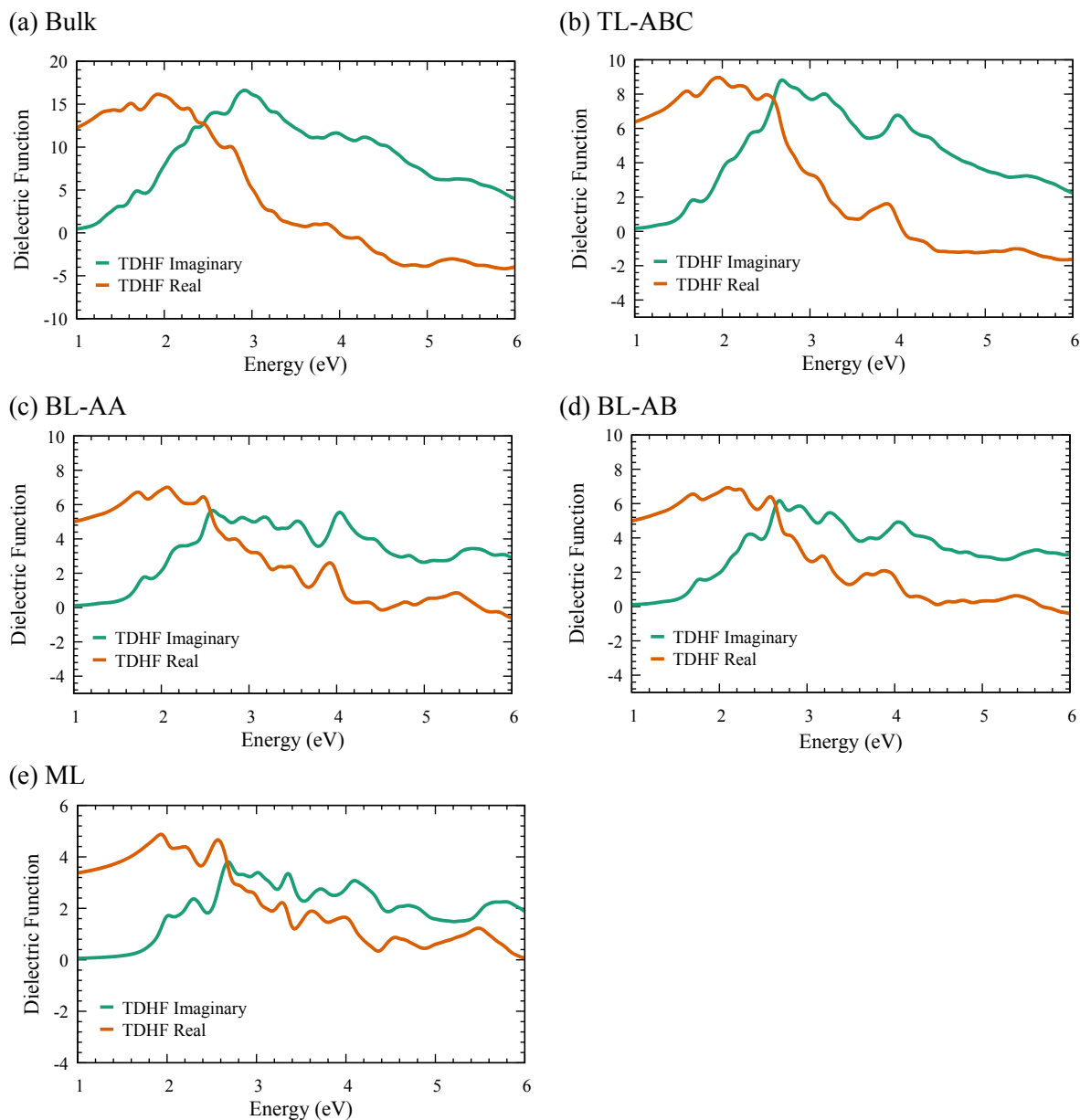
Figure S10 Calculated in-plane dielectric functions of monolayer, bilayer, trilayer and bulk $In_2Ge_2Te_6$ crystals using the time-dependent Hartree-Fock (TDHF) method.

References

[S1] Blochl, P. E. Projector Augmented-Wave Method. *Phys. Rev. B* **1994**, *50*, 17953.

[S2] Hafner, J. Ab-Initio Simulations of Materials Using VASP: Density-Functional Theory and Beyond. *J. Comput. Chem.* **2008**, *29*, 2044–2078.

[S3] Perdew, J. P.; Burke, K.; Ernzerhof, M. Generalized Gradient Approximation Made Simple. *Phys. Rev. Lett.* **1996**, *77*, 3865.

[S4] Dudarev, S. L.; Botton, G. A.; Savrasov, S. Y.; Humphreys, C. J.; Sutton, A. P. Electron-energy-loss Spectra and the Structural Stability of Nickel Oxide: An LSDA+U Study. *Phys. Rev. B* **1998**, *57*, 1505–1509.

[S5] Grimme, S.; Antony, J.; Ehrlich, S.; Krieg, H. A Consistent and Accurate Ab Initio Parametrization of Density Functional Dispersion Correction (DFT-D) for the 94 Elements H-Pu. *J. Chem. Phys.* **2010**, *132*, 154104.

[S6] Paier, J.; Marsman, M.; Hummer, K.; Kresse, G.; Gerber, I. C.; Ángyán, J. G. Screened Hybrid Density Functionals Applied to Solids. *J. Chem. Phys.* **2006**, *124*, 154709.

[S7] Bardeen, J.; Shockley, W. Deformation potentials and mobilities in non-polar crystals. *Phys. Rev.* **1950**, *80*, 72.

[S8] Qiao, J.; Kong, X.; Hu, Z.-X.; Yang, F.; Ji, W. High-Mobility Transport Anisotropy and Linear Dichroism in Few-Layer Black Phosphorus. *Nat. Commun.* **2014**, *5*, 4475.

[S9] Dai, J.; Zeng, X. C. Titanium Trisulfide Monolayer: Theoretical Prediction of a New Direct-Gap Semiconductor with High and Anisotropic Carrier Mobility. *Angew. Chem.* **2015**, *127*, 7682–7686.

[S10] Jing, Y.; Ma, Y.; Li, Y.; Heine, T. GeP$_3$: A Small Indirect Band Gap 2D Crystal with High Carrier Mobility and Strong Interlayer Quantum Confinement. *Nano Lett.* **2017**, *17*, 1833–1838.

[S11] Fonari, A.; Sutton, C. Effective Mass Calculator for Semiconductors. 2015.

[S12] Kresse, G.; Furthmüller, J.; Hafner, J. Ab Initio Force Constant Approach to Phonon Dispersion Relations of Diamond and Graphite. *EPL* **1995**, *32*, 729.

[S13] Parlinski, K.; Li, Z. Q.; Kawazoe, Y. First-Principles Determination of the Soft Mode in Cubic ZrO_2. *Phys. Rev. Lett.* **1997**, *78*, 4063–4066.

[S14] Togo, A.; Tanaka, I. First Principles Phonon Calculations in Materials Science. *Scripta Mater.* **2015**, *108*, 1–5.

[S15] Nosé, S. A Unified Formulation of the Constant Temperature Molecular Dynamics Methods. *J. Chem. Phys.* **1984**, *81*, 511–519.

[S16] Hoover, W. G. Canonical Dynamics: Equilibrium Phase-Space Distributions. *Phys. Rev. A* **1985**, *31*, 1695.

[S17] King-Smith, R.; Vanderbilt, D. Theory of Polarization of Crystalline Solids. *Phys. Rev. B* **1993**, *47*, 1651.

[S18] Saha, S.; Sinha, T.; Mookerjee, A. Electronic Structure, Chemical Bonding, and Optical Properties of Paraelectric $BaTiO_3$. *Phys. Rev. B* **2000**, *62*, 8828.

[S19] Gajdoš, M.; Hummer, K.; Kresse, G.; Furthmüller, J.; Bechstedt, F. Linear Optical Properties in the Projector-Augmented Wave Methodology. *Phys. Rev. B* **2006**, *73*, 045112.

[S20] Paier, J.; Marsman, M.; Kresse, G. Dielectric Properties and Excitons for Extended Systems from Hybrid Functionals. *Phys. Rev. B* **2008**, *78*, 121201.

[S21] Shockley, W.; Queisser, H. J. Detailed Balance Limit of Efficiency of p-n Junction Solar Cells. *J. Appl. Phys.* **1961**, *32*, 510–519.

[S22] Yu, L.; Zunger, A. Identification of Potential Photovoltaic Absorbers Based on First-Principles Spectroscopic Screening of Materials. *Phys. Rev. Lett.* **2012**, *108*, 068701.

[S23] Shockley, W.; Read, W. T. Statistics of the Recombinations of Holes and Electrons. *Phys. Rev.* **1952**, *87*, 835–842.

[S24] Trupke, T.; Green, M. A.; Wurfel, P.; Altermatt, P. P.; Wang, A.; Zhao, J.; Corkish, R. Temperature dependence of the radiative recombination coefficient of intrinsic crystalline silicon. *J. Appl. Phys.* **2003**, *94*, 4930.

[S25] Richter, A.; Glunz, S. W.; Werner, F.; Schmidt, J.; Cuevas, A. Improved quantitative description of Auger recombination in crystalline silicon. *Phys. Rev. B* **2012**, *86*.

[S26] Bercx, M.; Sarmadian, N.; Saniz, R.; Partoens, B.; Lamoen, D. First-principles analysis of the spectroscopic limited maximum efficiency of photovoltaic absorber layers for CuAu-like chalcogenides and silicon. *Phys. Chem. Chem. Phys.* **2016**, *18*, 20542–20549.

[S27] Adachi, S. *Optical Constants of Crystalline and Amorphous Semiconductors*; Springer US, 1999.

[S28] Green, M. A.; Keevers, M. J. Optical Properties of Intrinsic Silicon at 300 K. *Prog. Photovoltaics Res. Appl.* **1995**, *3*, 189–192.

[S29] Lefèvre, R.; Berthebaud, D.; Lebedev, O.; Pérez, O.; Castro, C.; Gascoin, S.; Chateigner, D.; Gascoin, F. Layered Tellurides: Stacking Faults Induce Low Thermal Conductivity in the New $In_2Ge_2Te_6$ and Thermoelectric Properties of Related Compounds. *J. Mater. Chem.A* **2017**, *5*, 19406–19415.

[S30] Ziambaras, E.; Kleis, J.; Schröder, E.; Hyldgaard, P. Potassium Intercalation in Graphite: A Van der Waals Density-Functional Study. *Phys. Rev. B* **2007**, *76*, 155425.

[S31] Zacharia, R.; Ulbricht, H.; Hertel, T. Interlayer Cohesive Energy of Graphite from Thermal Desorption of Polyaromatic Hydrocarbons. *Phys. Rev. B* **2004**, *69*, 155406.

[S32] Lv, J.; Xu, M.; Lin, S.; Shao, X.; Zhang, X.; Liu, Y.; Wang, Y.; Chen, Z.; Ma, Y. Direct-Gap Semiconducting Tri-layer Silicene with 29% Photovoltaic Efficiency. *Nano Energy* **2018**, *51*, 489–495.

[S33] NREL, Research Cell Record Efficiency Chart. 2019; `https://www.nrel.gov/pv/assets/pdfs/pv-efficiency-chart.20190103.pdf`.

[S34] Aspnes, D. E.; Studna, A. A. Dielectric functions and optical parameters of Si, Ge, GaP, GaAs, GaSb, InP, InAs, and InSb from 1.5 to 6.0 eV. *Phys. Rev. B* **1983**, *27*, 985–1009.